

## The long-distance charge transfer process in ferrocene-based MOFs with FeO<sub>6</sub> clusters boosts photocatalytic CO<sub>2</sub> chemical fixation

Honggang Zhang<sup>a</sup>, Shenghe Si<sup>a</sup>, Guangyao Zhai<sup>a</sup>, Yujie Li<sup>a</sup>, Yuanyuan Liu<sup>a,\*</sup>, Hefeng Cheng<sup>a</sup>, Zeyan Wang<sup>a</sup>, Peng Wang<sup>a</sup>, Zhaoke Zheng<sup>a</sup>, Ying Dai<sup>b</sup>, Terence Xiaoteng Liu<sup>c</sup>, Baibiao Huang<sup>a,\*</sup>

<sup>a</sup> State Key Laboratory of Crystal Materials, Shandong University, Jinan 250100, PR China

<sup>b</sup> School of Physics, Shandong University, Jinan 250100, PR China

<sup>c</sup> Faculty of Engineering and Environment, Northumbria University, Newcastle upon Tyne NE1 8ST, United Kingdom



### ARTICLE INFO

#### Keywords:

Ferrocene  
Metal organic frameworks  
Charge transfer process  
Photocatalysis  
CO<sub>2</sub> cycloaddition

### ABSTRACT

Metal nodes and organic ligands are important structural units of MOFs, and their properties can profoundly affect the photocatalytic activity. Herein, two ferrocene-based MOFs with FeO<sub>6</sub> or AlO<sub>6</sub> clusters as the metal nodes and 1,1'-ferrocenedicarboxylic acid (H<sub>2</sub>FcDC) as the ligands were successfully synthesized. Comparing with normal organic ligands, ferrocene ligands have longer-lived photogenerated charges due to metal-to-ligand charge transfer (MLCT) process, leading to a better photocatalytic activity of the corresponding ferrocene-based MOFs. In addition, the FeO<sub>6</sub> clusters are able to further accept the photogenerated electrons from ferrocene ligands compared to the inert AlO<sub>6</sub> clusters, allowing a long-distance charge transfer process, namely the proposed metal-to-ligand-to-metal charge transfer (MLMCT) process, which results in a better performance towards photocatalytic CO<sub>2</sub> cycloaddition reaction. This work sheds a light on designing MOFs using ferrocene ligands with high photocatalytic activity.

### 1. Introduction

Metal organic frameworks (MOFs), composed of organic ligands and metal nodes (including metal ions or metal clusters) connected through coordination bonds, are an emerging class of porous hybrid materials, which have gained great attention in the field of photocatalysis owing to their unique properties, such as ultrahigh surface area, structural and functional tunability and flexibility of modification [1–8]. However, due to the presence of poorly conductive units or the mismatch of the frontier orbitals between ligands and metal nodes, most MOFs tend to exhibit inefficient photogenerated charge transfer process, which greatly limits the further application of MOFs in the field of photocatalysis [9–13]. Hence, it is of high significance to design pristine MOFs with efficient charge separation and good photocatalytic activity.

In recent years, some successful approaches to obtain new-type pristine MOFs with good charge transfer capability have been developed. For example, increasing the conjugation of organic ligands, such as porphyrins and triphenylene, has proven to be an effective approach to enhance the charge transfer process [14,15]. Furthermore,

coordination between metal and ligand containing heteroatoms (such as N and S atoms) was proved to have the function of improving electrical conductivity of MOFs as well [16–18]. However, the reported approaches are still limited to the above cases and finding new solutions to obtain pristine MOFs with good charge transfer capability is of great significance. Ferrocene and its derivatives display high reversible redox properties and outstanding electrochemical activity [19–22]. Therefore, MOFs composed of ferrocene ligands are expected to display high charge transfer efficiency. In fact, some ferrocene-based MOFs have been reported, but there are few studies on photocatalytic activities for ferrocene-based MOFs that can be found in the literature [20,23–26].

In this work, we constructed two ferrocene-based MOFs, denoted as Fe-FcDC and Al-FcDC, with FeO<sub>6</sub> and AlO<sub>6</sub> clusters as metal nodes respectively. FeO<sub>6</sub> clusters in MOFs are well known to be reduced from Fe(III) to Fe(II) by the photogenerated electrons under light irradiation. [27–29] Therefore, it is meaningful to study the photophysical properties of FeO<sub>6</sub> clusters and ferrocene ligands constructed MOFs. On the other hand, AlO<sub>6</sub> clusters are reported to be an insulator, which is totally different from the FeO<sub>6</sub> counterparts [30]. As expected, our results first

\* Corresponding authors.

E-mail addresses: [yliu@sdu.edu.cn](mailto:yliu@sdu.edu.cn) (Y. Liu), [bbhuang@sdu.edu.cn](mailto:bbhuang@sdu.edu.cn) (B. Huang).

suggest that the ferrocene-based MOFs display better performance for photocatalytic CO<sub>2</sub> chemical fixation compared with their homologues with H<sub>2</sub>BDC (terephthalic acid) as the organic ligands. Secondly, ferrocene-based MOFs display different photophysical process and a novel metal-to-ligand-to-metal charge transfer (MLMCT) process over Fe-FcDC is proposed based on both the experimental and theoretical results. Due to the longer charge transfer path and extended lifetime of photogenerated charge carriers, Fe-FcDC displays better photocatalytic performance than Al-FcDC. This work provides an alternative pathway to enhance charge transfer process of MOFs with an organometallic compound ligand.

## 2. Experimental section

### 2.1. Chemicals

All the chemicals were analytical grade, and used directly without further purification. 1,1'-ferrocenedicarboxylic acid (H<sub>2</sub>FcDC), and epichlorohydrin carbonate were purchased from Bidepharm. Iron chloride hexahydrate (FeCl<sub>3</sub>·6 H<sub>2</sub>O), aluminium sulfate octadecahydrate (Al<sub>2</sub>(SO<sub>4</sub>)<sub>3</sub>·18 H<sub>2</sub>O), sodium sulfate (Na<sub>2</sub>SO<sub>4</sub>), N,N'-dimethylformamide (DMF), acetic acid, ethyl acetate were purchased from Sinopharm Chemical Reagent Co. Epichlorohydrin and tetrabutylammonium bromide (TBAB) were purchased from Macklin.

### 2.2. Synthesis of catalysts Fe-FcDC

Fe-FcDC was prepared according to the reported literature with minor modification. [24]. Typically, FeCl<sub>3</sub>·6 H<sub>2</sub>O (0.540 g, 2 mmol) and H<sub>2</sub>FcDC (0.274 g, 1 mmol) were dissolved in 20 mL DMF in a 45 mL Teflon container. After sonication at ambient temperature for 20 min, the obtained homogeneous solution was heated to 130 °C for 12 h. After cooled naturally, the product was washed with DMF and ethanol to remove unreacted organic linkers, which was finally dried at 60 °C for 12 h.

### 2.3. Synthesis of Al-FcDC

The synthesis of Al-FcDC followed a modified procedure reported previously [19]. In a 10 mL Schleck tube, Al<sub>2</sub>(SO<sub>4</sub>)<sub>3</sub>·18 H<sub>2</sub>O (0.133 g, 0.2 mmol) and H<sub>2</sub>FcDC (0.055 g, 0.2 mmol) were dissolved in a mixture containing DMF (2 mL) and water (2 mL). After 0.1 mL acetic acid was added, the tube was heated at 95 °C for 90 min under stirring. After that, the tube was naturally cooled to room temperature, and the precipitate was filtered and washed several times with DMF and water. The product was finally dried at 60 °C for 12 h.

### 2.4. Synthesis of Fe-BDC and Al-BDC

Fe-BDC and Al-BDC are also called MIL-53(Fe) and MIL-53(Al), which have the same crystal structure. In a typical process, terephthalic acid (0.166 g, 1 mmol) and FeCl<sub>3</sub>·6 H<sub>2</sub>O (0.270 g, 1 mmol) or Al(NO<sub>3</sub>)<sub>3</sub>·9 H<sub>2</sub>O (0.375 g, 1 mmol) were mixed in 20 mL DMF and sonication for 20 min. Then, the precursor solution was introduced into a 45 mL Teflon container and kept at 150 °C for 24 h. After cooled naturally, the product was collected and dried 60 °C for 12 h.

### 2.5. Characterizations

The X-ray diffraction patterns (XRD) of the samples were recorded on an X-ray powder diffraction (Bruker AXS D8, Cu K $\alpha$  radiation). Fourier transform infrared (FT-IR) spectra were performed with a Bruker ALPHA-T spectrometer. The X-ray photoelectron spectra (XPS) were obtained on a Thermo Scientific K-Alpha and the C 1 s peak at 284.8 eV was used to calibrate the peak position. The specific surface area, pore-size distribution and pore volume of the samples were detected by a

Micromeritics analyzer (ASAP Kubo X1000) at liquid nitrogen temperature. The CO<sub>2</sub> adsorption curves were measured by a Builder PCA-1100 gas adsorption analyzer. The thermogravimetric (TG) and differential scanning calorimeter (DSC) curves were recorded using a synchronous thermal analyzer (TA, SDTQ600) in the air. The micro-morphologies of the samples were recorded by a schottky field emission scanning electron microscopy (SEM, G300 FE-SEM System). The UV/Vis diffuse reflectance spectra (DRS) were characterized by a Shimadzu UV 2600i recording spectrophotometer with BaSO<sub>4</sub> as the reference. The Hall Effect was recorded by Quantum Design-PPMS-9. The steady photoluminescence (PL) spectra were determined by an Edinburgh Instruments FLS1000 under 250 nm excitation at room temperature. The in situ electron paramagnetic resonance (EPR) measurements were performed with Bruker EMXplus-6/1 at the temperature of 100 K. The real-time temperature of the reaction system was monitored by an infrared thermal imaging thermometer (HM-TPH11-3AXF). The temperature programmed desorption (TPD) of NH<sub>3</sub> measurement were carried out in Helium flow with a heating rate of 10 °C/min up to 300 °C and the released NH<sub>3</sub> was detected by an Auto Chem II 2920 with a TCD detector. The in situ FT-IR spectra were conducted using the Bruke Tensor II FTIR NEXUS spectrometer equipped with an in situ diffuse reflectance cell.

### 2.6. Electrochemical measurements

The electrochemical measurements were carried out using an electrochemical workstation (CHI660E C18532) with a standard three-electrode system and the light source was a 300 W Xe lamp coupled with an AM 1.5 solar simulator. The catalyst-coated FTO, Pt foil and Ag/AgCl (in saturated KCl) were used as the working electrode, counter electrode and reference electrode, respectively, and Na<sub>2</sub>SO<sub>4</sub> (0.1 M) solution acted as the electrolyte. The working electrode was prepared as follows: 10 mg catalyst was dispersed in 2 mL of ethanol containing 20  $\mu$ L Nafion solution. After the mixture was sonicated for 2 h to a homogeneous suspension, it was dropped onto a 1 × 2 cm<sup>2</sup> clean FTO glass. The FTO glass was dried at 100 °C for one hour and a uniform electrode was obtained. All the measurements were performed at a voltage of 0 V (vs Ag/AgCl).

### 2.7. Catalytic CO<sub>2</sub> cycloaddition reaction

In a typical procedure, 15 mg as-synthesized catalyst was added into a closed quartz glass reactor and the reactor was purged with CO<sub>2</sub> gas for 20 min. After that, 3 mL epichlorohydrin and 0.3 mmol TBAB (tetrabutylammonium bromide) were injected into the reactor. A 1 L balloon filled with pure CO<sub>2</sub> gas was connected to the reactor to keep the internal pressure at 1 atm during the process of the reaction. The suspension was irradiated by a 300 W Xe lamp (CEL-HXF300) and the light source was located at a distance of 15 cm above the reactor. After the reaction, the resulting solution was extracted by a mixed solution of ethyl acetate and water (V/V, 1/1), and the product in the upper ethyl acetate was detected by gas chromatography (GC-2030, SH-Rtx-5) equipped with an FID detector. The turnover number (TON) is determined as follows: TON = product (mmol)/active sites (mmol) and each ferrocene ligand is regarded as an isolated active site.

### 2.8. Theoretical calculations

All calculations were based on the density functional theory (DFT) and performed with the Vienna ab initio simulation package (VASP) code [31,32]. The exchange and correlation energy functional was expressed in the GGA-PBE [33]. The projector-augmented wave method was used to describe the interactions between ions and electrons [34, 35]. The valence electrons were solved in the plane-wave basis with a cutoff energy of 450 eV. The convergence criteria for the energy calculation and structure optimization were set to  $1.0 \times 10^{-6}$  eV and a

force tolerance of 0.05 eV/Å, respectively. The Brillouin-zone integration was performed using a  $1 \times 3 \times 3$  Gamma-centered k-point mesh with Gaussian smearing set to 0.05 eV for Fe-FcDC and  $3 \times 2 \times 2$  Gamma-centered k-point mesh for Al-FcDC, respectively. The spin polarization is considered for all structures and the optimized structures for the calculations are shown in Fig. S1 and S2.

### 3. Results and discussion

#### 3.1. DFT of charge transfer

As an organometallic compound with reversible redox activity, ferrocene compounds are photosensitive, capable of charge transfer between central Fe atom and cyclopentadienyl rings under light irradiation. In order to clarify the valence electron distribution, the electron density diagrams of the front-line orbitals of H<sub>2</sub>FcDC in two extreme conformations (i.e. 0° and 180°) are shown in Fig. 1a-b. The HOMO (the highest occupied molecular orbital) is concentrated in the 3d orbital of central Fe atom with a small contribution from the cyclopentadienyl rings [36]. As for the LUMO (the lowest unoccupied molecular orbital), the main part of the electron density is occupied by cyclopentadienyl rings-related atoms, while the Fe atom-related orbitals show only a subtle contribution, which is not related to the rotational conformation of ferrocene. Therefore, the photogenerated charge transfer process in H<sub>2</sub>FcDC is dominated by the metal-to-ligand charge transfer (MLCT) process.

After clarifying the charge transfer process on ferrocene ligands, density of states (DOS) were further calculated to reveal the effect of different metal-oxygen clusters on the electronic structure of ferrocene-based MOFs. As displayed in Fig. 1c-d, the Fermi levels of both Fe-FcDC and Al-FcDC locate on the HOMO side, indicating that they exhibit p-type semiconductor behavior [37]. Both the HOMO and LUMO for Al-FcDC, with an energy gap of 1.86 eV, are mainly composed of Fe and C atoms in the ferrocene units, and the AlO<sub>6</sub> clusters contribute little to the frontier orbital, suggesting that AlO<sub>6</sub> clusters cannot accept or donate electrons and the excitation process mainly occurs in the ferrocene ligands, which is well consistent with previous reports on Al-based MOFs.

For Fe-FcDC, it can be obviously pointed out that the FeO<sub>6</sub> clusters contribute to the frontier orbital with a narrow band gap and the clearly electron density near the Fermi level implies a good conductivity. Besides that, the ferrocene units exhibit a prominent contribution to the deeper energy orbital, with an energy gap of about 1.93 eV to the LUMO (contributed by both ferrocene units and FeO<sub>6</sub> clusters), suggesting that the photogenerated charges have a probability to be transported into the FeO<sub>6</sub> clusters as long as the ferrocene ligands in Fe-FcDC can be excited [13,38]. In fact, the above process can indeed take place, which will be demonstrated later in the experimental characterization section. This indicates that the photogenerated charges over Fe-FcDC possess a longer transport distance compared to Al-FcDC due to the matched energy level orbitals of metal nodes and ligands, which is expected to result in higher photocatalytic activity.

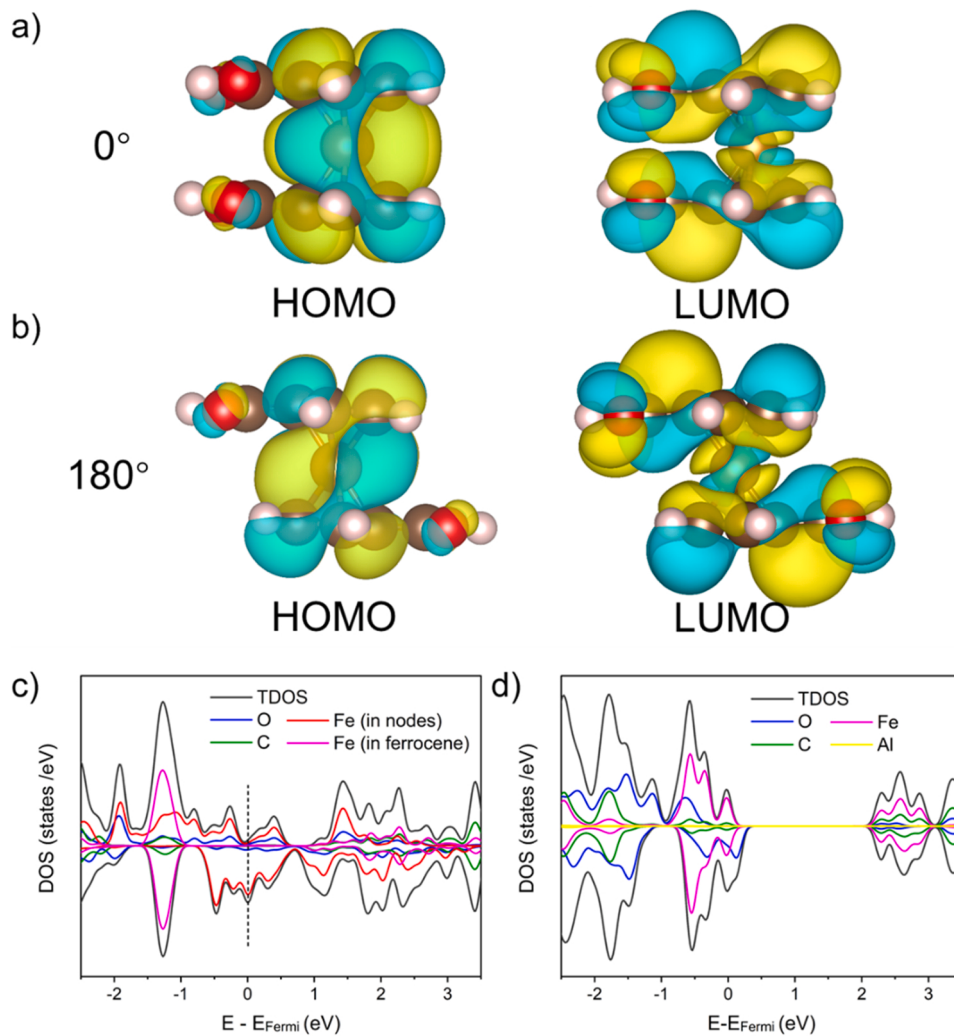


**Fig. 1.** The LUMO and HOMO orbitals calculated for H<sub>2</sub>FcDC in (a) 0° and (b) 180° conformations. Total DOS and partial DOS of (c) Fe-FcDC and (d) Al-FcDC.

### 3.2. Characterization of catalysts

To check above inference, both Fe-FcDC and Al-FcDC were synthesized by solvothermal method. As presented in Fig. 2a, the X-ray diffraction (XRD) spectra of Fe-FcDC and Al-FcDC show the same characteristic peaks as previously reported and no extra peaks can be observed, suggesting the successful synthesis of the samples with a good purity. Fourier transform infrared (FT-IR) spectra (Fig. 2b and Fig. S3) further justify the successful preparation of Fe-FcDC and Al-FcDC. Compared with H<sub>2</sub>FcDC, both Fe-FcDC and Al-FcDC display similar change trend. In detail, the asymmetric stretching vibration peak of C=O belonging to the carboxyl group (-COOH) for H<sub>2</sub>FcDC (around 1683 cm<sup>-1</sup>) shifts to shorter wavenumber for carboxylate anions (-COO<sup>-</sup>) in MOFs (around 1570 cm<sup>-1</sup>), and the stretching vibration peak of C-O in MOFs disappears from 1300 cm<sup>-1</sup> compared with the ligand H<sub>2</sub>FcDC, indicating that H<sub>2</sub>FcDC coordinates to the metal-oxygen clusters by deprotonation of the carboxyl group. In addition, the characteristic peaks (around 1490 cm<sup>-1</sup> and 1170 ~ 1200 cm<sup>-1</sup>) of cyclopentadienyl (Cp) rings in ferrocene units are well retained, suggesting the ferrocene structure is preserved in MOFs [39].

The X-ray photoelectron spectra (XPS) were further performed to explore the elemental composition and chemical states. The survey spectra for all samples are shown in Fig. S4 and no additional elements except the ones that composing of the material can be detected. For the high-resolution of Fe 2p spectra (Fig. 3c), the two peaks located at around 708.3 eV and 721.1 eV for H<sub>2</sub>FcDC belong to the Fe 2p<sub>3/2</sub> and Fe 2p<sub>1/2</sub>, respectively, suggesting that the valence state of Fe shows a typical Fe(II) [40,41]. For Fe-FcDC, compared to the ligand H<sub>2</sub>FcDC, a series of signal peaks belonging to Fe(III) can be clearly observed [42]. Fe(III) can also be observed for Al-FcDC, which may be caused by unavoidable surface oxidation. Besides, as shown in Fig. S5, the Al 2p spectrum clearly indicates the presence of Al element in Al-FcDC, with a peak at 75.6 eV belonging to the Al-O species [43].

The optical properties were further measured by UV-vis diffuse reflectance spectra (DRS). As presented in Fig. S6, H<sub>2</sub>FcDC exhibits two

absorption bands at around 315 nm and 460 nm, which is the unique dual optical absorption feature of ferrocene complexes [19,23]. For Al-FcDC, the two characteristic absorption bands are remained with the position slightly shifted towards longer wavelengths. However, this unique optical property cannot be clearly observed for Fe-FcDC due to the strong absorption of Fe-O bonds in this region. The band gap (Eg) is determined to be 1.81 eV for Fe-FcDC and 1.87 eV for Al-FcDC based on the Tauc plots (Fig. S7), which is in good agreement with the calculated ones. Besides, as displayed in Fig. S8, the XPS valence band spectra of Fe-FcDC and Al-FcDC show that the valence band potential (E<sub>VB</sub>) is located at about 0.34 eV and 0.52 eV, respectively. According to the equation E<sub>g</sub> = E<sub>VB</sub> - E<sub>CB</sub>, the corresponding E<sub>CB</sub> is estimated to be at -1.47 eV for Fe-FcDC and -1.35 eV for Al-FcDC. The flat-band potentials could be determined to be 0.14 eV for Fe-FcDC and 0.32 eV for Al-FcDC by the Mott-Schottky plots (Fig. S9), the negative slope indicates that both Fe-FcDC and Al-FcDC are p-type semiconductors and the valence band position tends to be about 0.2 eV more positive than the flat-band potential for p-type semiconductors, which is consistent with above result. What's more, the morphology and the energy-dispersive spectrometry (EDS) elemental mapping (Fig. S10), thermogravimetric (TG) and differential scanning calorimeter (DSC) curves (Fig. S11) and the Brunauer-Emmett-Teller (BET) surface areas (Fig. S12) all indicate the successful preparation of Fe-FcDC and Al-FcDC.

### 3.3. Experimental investigation of charge transfer

After the successful synthesis of ferrocene-based MOFs, the charge transfer processes were further investigated to verify the theoretical findings. Besides, in order to verify the superiority of ferrocene ligands, Fe-BDC and Al-BDC were synthesized as comparison samples with normal organic ligands (Fig. S13). Steady photoluminescence (PL) spectra were applied to confirm the difference in charge separation efficiency. As plotted in Fig. 3a, the maximum fluorescence emission of Al-FcDC and Fe-FcDC is red-shifted compared to the H<sub>2</sub>FcDC ligand, which

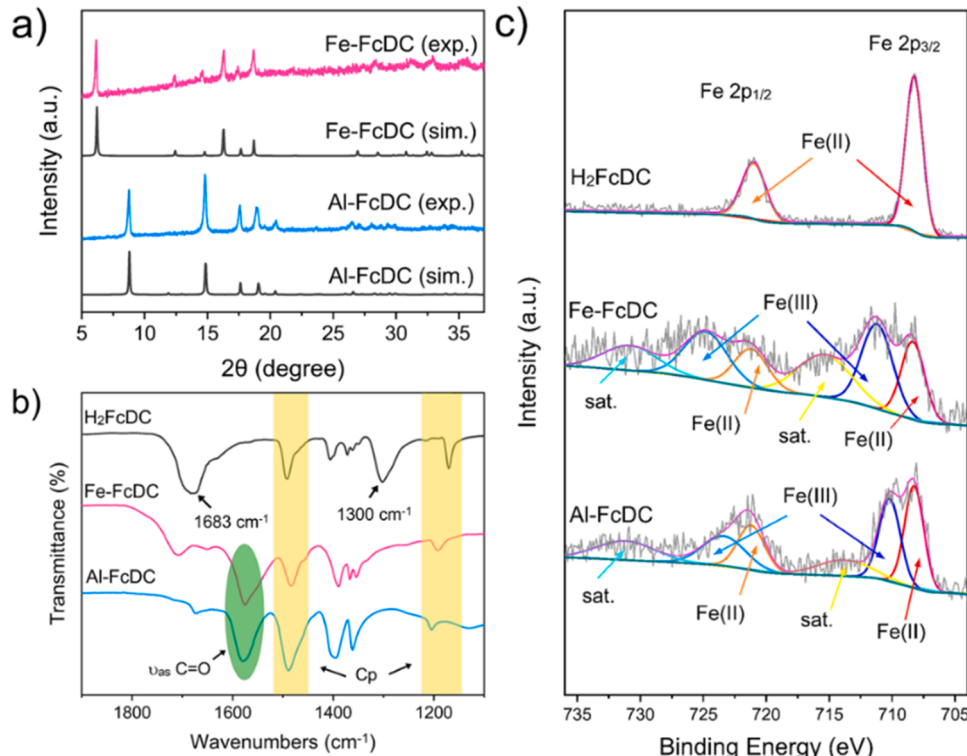


**Fig. 2.** (a) XRD patterns of Fe-FcDC and Al-FcDC; (b) FT-IR spectra and (c) XPS spectra for Fe 2p of H<sub>2</sub>FcDC, Fe-FcDC and Al-FcDC.

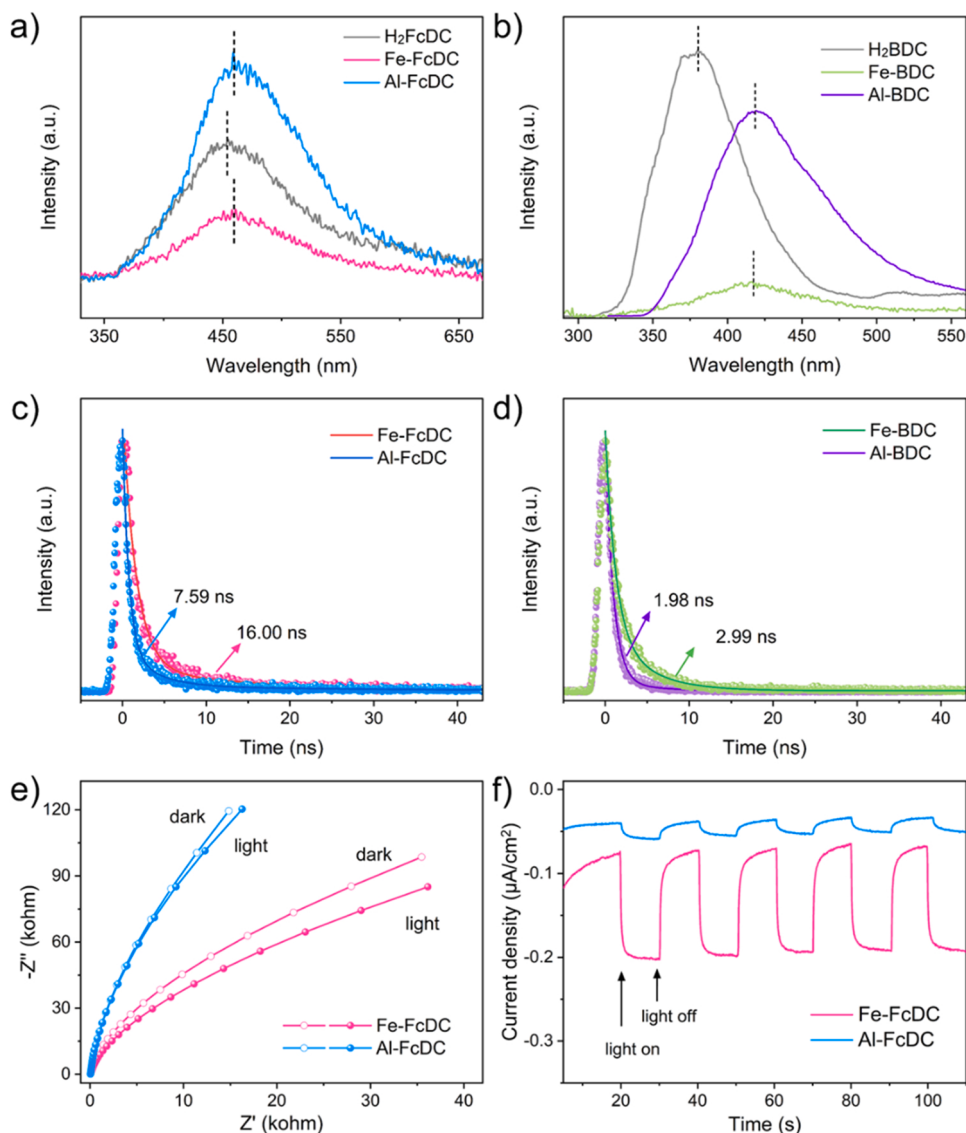


**Fig. 3.** The steady PL decay spectra of (a) H<sub>2</sub>FcDC, Fe-FcDC and Al-FcDC, and (b) H<sub>2</sub>BDC, Fe-BDC and Al-BDC. The time-resolved PL spectra of (c) Fe-FcDC and Al-FcDC, and (d) Fe-BDC and Al-BDC; (e) The EIS plots and (f) the transient photocurrent responses of Fe-FcDC and Al-FcDC.

can be interpreted by the coordination between the carboxyl group and the metal. The similar emission peaks for Fe-FcDC and Al-FcDC with the H<sub>2</sub>FcDC ligand suggest that both ferrocene ligand and ferrocene-based MOFs can be excited upon light irradiation leading to the production of electron hole pairs. However, the emission intensity for Fe-FcDC significantly decreases, further suggesting that the recombination of photogenerated charge carriers is greatly suppressed, which may be due to that a new electron transfer pathway appears [44,45]. Compared with Fe-FcDC, the photogenerated electron-hole pairs are localized in the ferrocene units over Al-FcDC, which enhances the recombination possibility and consequently leads to a higher emission intensity. Additionally, Fe-BDC and Al-BDC have similar trends in fluorescence emission peaks compared to H<sub>2</sub>BDC ligand, confirming the effect of metal nodes on the separation of photogenerated carriers (Fig. 3b).

The advantages of ferrocene ligands in photocatalysis were further demonstrated by time-resolved photoluminescence decay spectra to monitor the photogenerated carrier lifetime, and the results are shown in Fig. 3c-d. The curves are fitted with tri-exponential decay for ferrocene-based MOFs and bi-exponential decay for typical MOFs (Table S1). Ferrocene-based MOFs (16.00 ns for Fe-FcDC and 7.59 ns Al-FcDC) have a longer average fluorescence lifetime than typical MOFs

with H<sub>2</sub>BDC ligand (2.99 ns for Fe-BDC and 1.98 ns Al-BDC), signifying that ferrocene-based MOFs exhibit a more efficient electron-hole separation due to the MLCT process. Moreover, Fe-FcDC displays a much longer lifetime of the photogenerated charges than does Al-FcDC due to FeO<sub>6</sub> clusters can accept the photogenerated electrons from ferrocene ligands. Therefore, it is reasonable to predict Fe-FcDC exhibits a higher charge separation efficiency and better photocatalytic activity than Al-FcDC. Besides, whether the MOFs consisted of ferrocene ligands or normal ligands, the Fe-based MOFs have the longer fluorescence lifetime than the corresponding Al-based MOFs, indicating that the suitable metal nodes possess a positive role in enhancing the carrier separation efficiency.

Photo-electrochemical tests were also carried out to check the effect of different metal clusters on the transfer and separation efficiency of photogenerated electron-hole pairs. The electrochemical impedance spectra (EIS) plots (Fig. 3e) demonstrate that both Fe-FcDC and Al-FcDC show a smaller arc radius under light than that in the dark, suggesting light irradiation could decrease the resistance due to the generation of free electrons and holes [46]. To obtain a more intuitive impression, the data were simulated by equivalent circuit diagram (Fig. S14). Obviously, Fe-FcDC displays a larger decrease (31.4%) than does Al-FcDC (5.6%),

confirming the much more efficient photogenerated electrons transfer and separation of the former, revealing the positive effect of  $\text{FeO}_6$  clusters on the transport of photogenerated electrons. The Hall Effect was also used to verify the resistivity of the Fe-FcDC and Al-FcDC. As displayed in Table S2, Fe-FcDC has a lower resistivity value and a higher carrier mobility than Al-FcDC, which is consistent with the above trend.

The transient photocurrent response were further applied to determine the separation efficiency and the results also suggest a similar conclusion. As shown in Fig. 3f, the photocurrent of Fe-FcDC is significantly higher than that of Al-FcDC. The cathodic photocurrent suggests that both Fe-FcDC and Al-FcDC are p-type semiconductors, agreeing well with the theoretical results. Furthermore, the electrochemical properties of the Fe-FcDC and Al-FcDC were further investigated by linear sweep voltammetry (LSV). As can be seen from Fig. S15, Fe-FcDC (0.55 V vs. Ag/AgCl) appears a lower oxidation potential than does Al-FcDC (0.57 V vs. Ag/AgCl) and the oxidation potential can be ascribed to the oxidation process of Fe(II) to Fe(III) in ferrocene ligands, suggesting that it is easier for the oxidation of ferrocene ligands in Fe-FcDC, which may be induced by the matched energy level orbitals of metal nodes and ligands as well.

To demonstrate the MLCT process more directly, the in situ EPR measurements were performed to record the free electron signal changes over Al-FcDC before and after light irradiation. As shown in Fig. S16, a peak related to  $\text{Fc}^+$  at a g value of 2.00 is significantly increased under light irradiation, which can be attributed to the conversion of Fe(II) to Fe(III) in ferrocene, demonstrating the MLCT process over ferrocene-based MOFs. Besides, the broad peak at  $g = 4.07$  displays no significant changes before and after light irradiation, which is attributed to the Fe(III) species formed by surface oxidation during the synthesis process [12,19,22].

#### 3.4. Mechanism of charge transfer

Based on above results and discussion, the charge generation and transfer process over ferrocene-based MOFs can be deduced as follows (Fig. 4). For both Fe-FcDC and Al-FcDC, the ferrocene ligands are responsible for light irradiation and the photogenerated electron can be transported from the central Fe atom to the cyclopentadienyl rings, which is defined as the MLCT process. Following this, the photogenerated electrons will be further transferred to the  $\text{FeO}_6$  clusters (MLMCT process) over Fe-FcDC, which prolongs the transmission distance of the photogenerated carriers and reduces the possibility of recombination. However, the photogenerated electron-hole pairs are localized in the ligand for Al-FcDC and easy to recombine. Therefore, it is reasonable to assume that Fe-FcDC displays better photocatalytic performance.

#### 3.5. Photocatalytic performance of catalysts

To check above consumption, solvent-free photocatalytic  $\text{CO}_2$  cycloaddition reaction over Fe-FcDC and Al-FcDC were investigated under mild conditions with epichlorohydrin as model substrate.  $\text{CO}_2$  cycloaddition reaction is an atom economy pathway to convert  $\text{CO}_2$  into value-added chemicals for  $\text{CO}_2$  chemical fixation [47,48]. As can be seen from Fig. 5a, Fe-FcDC exhibits a high efficiency with a TON value of 74.2 under full spectrum of light irradiation, while a TON value of 49.1 is obtained in the presence of Al-FcDC under the same conditions. After subtracting the yield contributed by the dark reaction, the TON value obtained over Fe-FcDC (43.6, the TON value is 30.6 in the dark) via the photochemical reaction is also higher than that over Al-FcDC (27.3, the TON value is 21.8 in the dark). To be explained, the rate of  $\text{CO}_2$  cycloaddition reaction in the dark is usually positively correlated with the Lewis acidity of the catalyst, which has been proved by  $\text{NH}_3\text{-TPD}$  experiments (Fig. S17) [49,50]. As a comparison, measurements of the photocatalytic  $\text{CO}_2$  cycloaddition reaction over Fe-BDC and Al-BDC were also performed. Consistent with above discussion, the TON values over both Fe-BDC and Al-BDC (7.0 and 3.3) under light irradiation are smaller than that of the corresponding ferrocene-based MOFs, confirming the advantages of ferrocene as ligands to construct MOFs photocatalysts.

To demonstrate the superiority of porous structure of MOFs in catalytic reactions, ferrocene (Fc) was used as the catalyst for  $\text{CO}_2$  cycloaddition reactions (Fig. 5a) and the TON value over ferrocene was only 13.3 under light irradiation. Besides, light shows a poor promotion effect for ferrocene compared to the ferrocene-based MOF and the TON value of the former is only 5.5 under light irradiation, which is even lower than that in the dark (7.8). Further controlled experiments were carried out to show the structure-effect relationship between the various components of the MOFs and the catalytic performance. As displayed in Fig. S18, when either ferrocene ligands,  $\text{Fe}_2\text{O}_3$  or  $\text{Al}_2\text{O}_3$  were used as the photocatalysts, the yields were much lower than the corresponding MOFs, which further confirms that the porous structure of MOFs plays an essential role in photocatalytic reaction.

#### 3.6. Exploration of $\text{CO}_2$ cycloaddition mechanism

According to our previous work and available reports, the mechanism of  $\text{CO}_2$  cycloaddition reaction under light irradiation can be attributed to the following two aspects, the activation of  $\text{CO}_2$  by photogenerated electrons and the acceleration of ring-opening of epoxide by photogenerated holes.[40,49–51] Photocatalytic  $\text{CO}_2$  reductions were conducted to investigate the activation ability for  $\text{CO}_2$  by ferrocene-based MOFs and the results are displayed in Fig. S19. Both Fe-FcDC and Al-FcDC show efficient  $\text{CO}_2$  reduction ability with CO as the major product, and the performance over Fe-FcDC (26.6  $\mu\text{mol}/(\text{g h})$ ) is better than that over Al-FcDC (21.7  $\mu\text{mol}/(\text{g h})$ ). No product can be

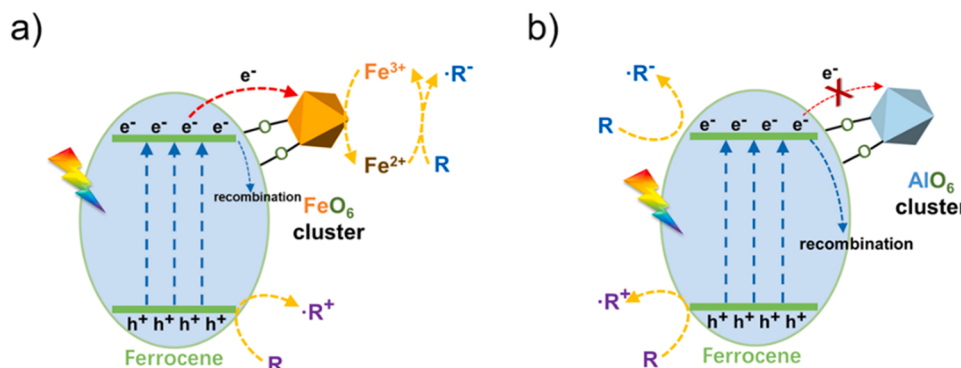


**Fig. 4.** Schematic diagram illustrating the proposed mechanism of charge transfer process over (a) Fe-FcDC and (b) Al-FcDC.

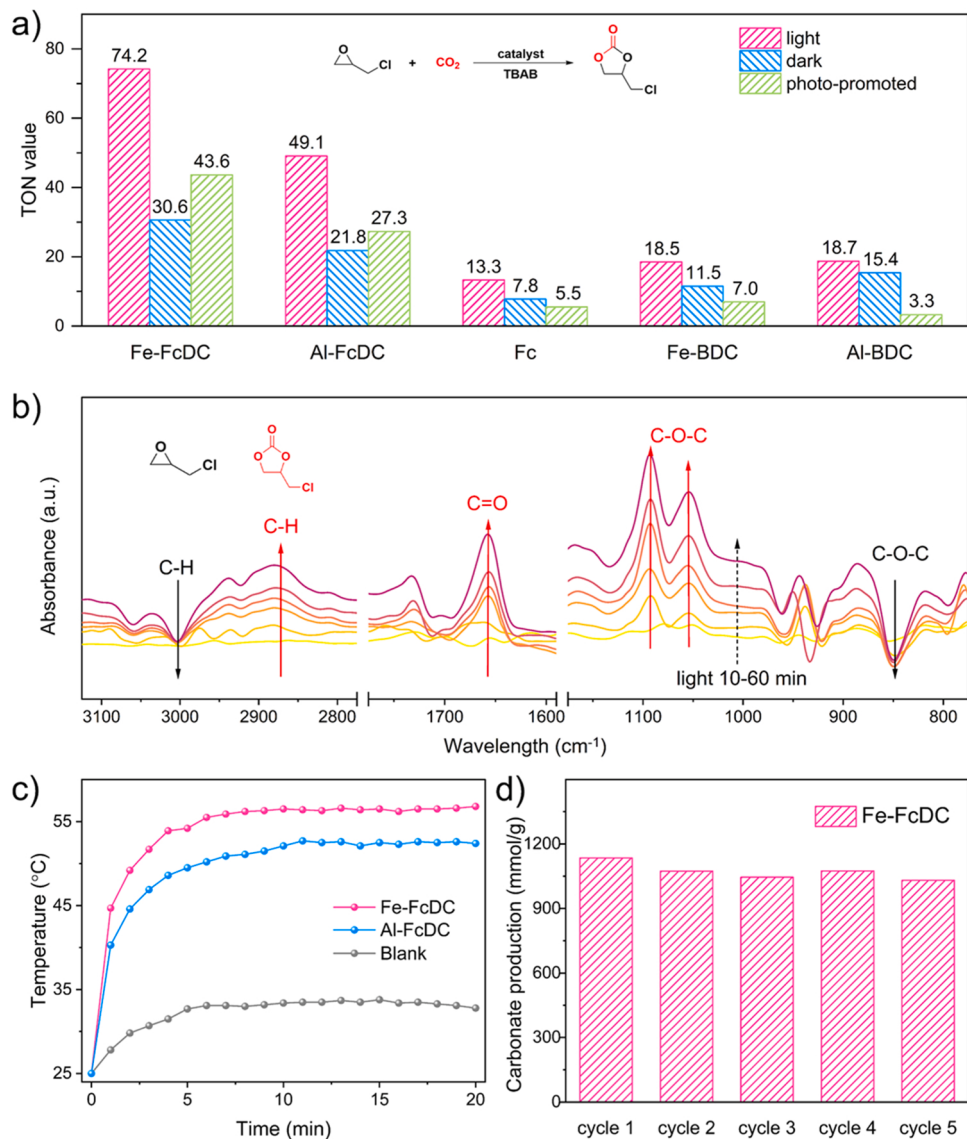


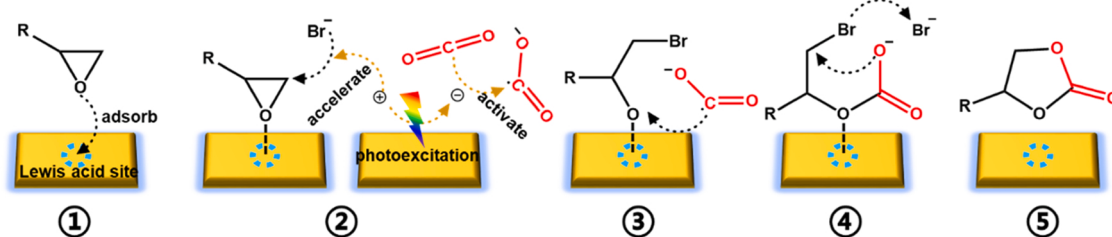
**Fig. 5.** (a) The turnover number for  $\text{CO}_2$  cycloaddition reaction within 4 h under different conditions; (b) The in situ FT-IR spectrum for detecting  $\text{CO}_2$  cycloaddition reaction over Fe-FcDC; (c) Photothermal effect of Fe-FcDC and Al-FcDC (the initial temperature is 25 °C) and (d) the stability test of Fe-FcDC.

detected in the absence of light irradiation, proving that the production of CO is initiated by the photocatalytic process over the catalysts. Besides, the  $\text{CO}_2$  adsorption isotherms show that the maximum adsorption capacity ( $P/P_0 = 1$ , 273 K) of the Fe-FcDC ( $22.6 \text{ cm}^3/\text{g}$ ) and Al-FcDC ( $20.1 \text{ cm}^3/\text{g}$ ) is closely similar (Fig. S20), therefore, the difference in photocatalytic performance between Fe-FcDC and Al-FcDC arises from the difference in charge separation efficiency rather than the ability to capture  $\text{CO}_2$ . The in situ FT-IR measurements were employed to more directly demonstrate the activation of  $\text{CO}_2$  under light irradiation. Two typical peaks ( $1720\text{--}1680 \text{ cm}^{-1}$  and  $1194 \text{ cm}^{-1}$ ) attributed to  $\bullet\text{CO}_2$  appear obviously under  $\text{CO}_2$  atmosphere and light irradiation (Fig. S21) [52]. The ring-opening intermediate products of epoxide can be detected by GC-MS when the substrate is styrene oxide (Fig. S22). As can be seen from Fig. S23, the TON values of the ring-opening intermediate products increase significantly under light irradiation, nearly twice as much as in the dark. Likewise, Fe-FcDC exhibits stronger enhancement than does Al-FcDC under light irradiation.

To investigate the mechanism of the  $\text{CO}_2$  cycloaddition reaction in detail, the in situ FT-IR measurements were performed to detect the changes in reactant and product functional group during photocatalytic process. As illustrated in Fig. 5b, a new characteristic absorption peak is

obviously apparent at  $1657 \text{ cm}^{-1}$  and grows stronger with time, which can be attributed to the  $\text{C}=\text{O}$  vibration of the product cyclic carbonate. Furthermore, the peaks of  $\text{C}-\text{O}-\text{C}$  bond in the product cyclic carbonate at around  $1054 \text{ cm}^{-1}$  and  $1092 \text{ cm}^{-1}$  accumulates over time, while the peak attributed to the  $\text{C}-\text{O}-\text{C}$  bond in the epoxide at around  $850 \text{ cm}^{-1}$  diminished. Besides, the vibrational peaks of  $\text{C}-\text{H}$  bond in epoxide (around  $3005 \text{ cm}^{-1}$ ) and cyclic carbonate (around  $2880 \text{ cm}^{-1}$ ) show a similar trend, demonstrating that the product cyclic carbonate is produced from the epoxide over time. [25,53].

Based on above results, we propose the following reaction steps of  $\text{CO}_2$  cycloaddition reaction over ferrocene-based MOFs (Scheme 1). The epoxide first adsorbs onto the Lewis acid site in ferrocene-based MOFs through O atom, which weakens the strength of  $\text{C}-\text{O}$  bond in the epoxides. Then, the Br ion in TBAB acts as the nucleophilic reagent to attack the C atom, resulting in the breakage of the  $\text{C}-\text{O}$  bond and the formation of the  $\text{C}-\text{Br}$  bond. Meantime, the photogenerated hole generated over ferrocene-based MOFs can also serve as Lewis acidic site to accelerate the production of ring-opening intermediate. The C atom in  $\text{CO}_2$  is linked to the O atom in ring-opening intermediate to constitute a new  $\text{C}-\text{O}$  bond. Accordingly, photogenerated electron is employed to activate the linear  $\text{CO}_2$  into a bent structure, which could reduce the space



**Scheme 1.** Proposed of photocatalytic  $\text{CO}_2$  cycloaddition reaction over ferrocene-based MOFs.

potential resistance and speed up the reaction. The final product cyclic carbonate is produced after cyclization reaction, while the  $\text{Br}^-$  ion is discharged and TBAB is regenerated.

### 3.7. Photo-driven $\text{CO}_2$ cycloaddition

For  $\text{CO}_2$  cycloaddition reaction, it is well known that high temperature is beneficial to further increase the rate of cycloaddition reaction [49,54]. In order to obtain a higher yield of epichlorohydrin carbonate, the photothermal effect of Fe-FcDC and Al-FcDC were further explored considering the strong absorption of Fe-FcDC and Al-FcDC in the entire visible light region (Fig. S6). The elevated temperature of the suspension containing Fe-FcDC was recorded by an infrared thermal imaging thermometer (Fig. 5c) and the temperature quickly increases to 56 °C within 10 min. For comparison, the temperature can only increase to 52 °C for the Al-FcDC suspension under the same conditions, which agrees well with the difference in light absorption. The temperature of the pure solution without any catalysts reaches less than 35 °C under the same conditions, proving the excellent photothermal effect of Fe-FcDC and Al-FcDC.

Therefore, the catalytic performance of photo-driven  $\text{CO}_2$  cycloaddition over Fe-FcDC was checked under full spectrum of light irradiation. An ultra-high yield (1135.0 mmol/g and TON=474.5, Table S3, Entry 1) of epichlorohydrin carbonate is obtained within 4 h, which is comparable with many other reported photothermal catalysts (Table S4), [25,40,47,51,55–59]. Further control experiments (Table S3) show that the yield of epichlorohydrin carbonate will be limited by the removal of either TBAB or catalyst, indicating that both the cocatalyst TBAB and the catalyst Fe-FcDC are very important for promoting the  $\text{CO}_2$  cycloaddition reaction. Besides, the performance of the catalyst does not decrease significantly within five parallel experiments (Fig. 5d). There is no noticeable difference between the powder XRD patterns (Fig. S24), FT-IR spectra (Fig. S25) and XPS spectra (Fig. S26) before and after the stability test, further verifying the excellent stability of Fe-FcDC, which is a prerequisite for its practical application. Moreover, the photo-driven  $\text{CO}_2$  cycloaddition reaction over Fe-FcDC was investigated with a wide range of substrate scopes and the results are summarized in Table S5. All the epoxides demonstrate a desirable conversion, suggesting the ideal substrate tolerance of Fe-FcDC.

## 4. Conclusion

In summary, we synthesized two ferrocene-based MOFs (Fe-FcDC and Al-FcDC) and investigated the effects of ferrocene ligands and metal nodes on the charge separation and photocatalytic performance by combining theoretical calculations with experimental investigations. It is found that, compared with typical MOFs with  $\text{H}_2\text{BDC}$  ligand, ferrocene-based MOFs display a more efficient charge transfer process due to the MLCT process in the ferrocene ligands, which enhances the photocatalytic performance towards photo-driven  $\text{CO}_2$  cycloaddition reactions. In addition, the  $\text{FeO}_6$  clusters can further accept electrons from ferrocene ligands compared to inert  $\text{AlO}_6$  clusters, and a novel metal-to-ligand-to-metal charge transfer (MLMCT) process was

proposed for Fe-FcDC to describe the long charge transfer path, which is believed to be beneficial for the separation of photogenerated carriers. In fact, Fe-FcDC displays a better photocatalytic performance than does Al-FcDC. This work provides an alternative guidance for the design and synthesis of novel organometallic compound-based MOFs with efficient photogenerated charge transfer process and photocatalytic activity.

## CRediT authorship contribution statement

**Honggang Zhang:** Conceptualization, Methodology, Formal analysis, Investigation, Writing – original draft, Visualization. **Shenghe Si:** Conceptualization, Formal analysis, Investigation. **Guangyao Zhai:** Methodology, Validation. **Yujie Li:** Methodology, Validation. **Yuanyuan Liu:** Formal analysis, Resources, Writing – review & editing, Supervision, Project administration, Funding acquisition. **Hefeng Cheng, Zeyan Wang, Peng Wang and Zhaoke Zheng:** Resources, Funding acquisition. **Ying Dai:** Resources, Visualization. **Terence Xiaoteng Liu:** Writing-Review & Editing, Funding acquisition. **Biaobai Huang:** Resources, Writing-Review & Editing, Supervision, Funding acquisition.

## Declaration of Competing Interest

The authors declare that they have no known competing financial interests or personal relationships that could have appeared to influence the work reported in this paper.

## Data Availability

Data will be made available on request.

## Acknowledgements

This work is financially supported by the National Key Research and Development Program of China (2020YFA0710301), National Natural Science Foundation of China (grant numbers 22172088, 51972195, 21832005, 21972078, 11374190), the Shandong Province Natural Science Foundation (ZR2020YQ16), the Royal Society International Exchanges Award (Grant No. IEC\NSFC\201008).

## Appendix A. Supporting information

Supplementary data associated with this article can be found in the online version at doi:10.1016/j.apcatb.2023.122909.

## References

- [1] Y. Wang, Z. Zhang, J. Li, Y. Yuan, J. Yang, W. Xu, P. An, S. Xi, J. Guo, B. Liu, J. Li, Two-dimensional-on-three-dimensional metal-organic frameworks for photocatalytic  $\text{H}_2$  production, *Angew. Chem. Int. Ed.* 61 (2022), e202211031.
- [2] T. Zhuo, Y. Song, G. Zhuang, L. Chang, S. Yao, W. Zhang, Y. Wang, P. Wang, W. Lin, T. Lu, Z. Zhang, H-Bond-mediated selectivity control of formate versus  $\text{CO}$  during  $\text{CO}_2$  photoreduction with two cooperative Cu/X sites, *J. Am. Chem. Soc.* 143 (2021) 6114–6122.

- [3] S. Guo, L.H. Kong, P. Wang, S. Yao, T.B. Lu, Z.M. Zhang, Switching excited state distribution of metal–organic framework for dramatically boosting photocatalysis, *Angew. Chem. Int. Ed.* 61 (2022), e202206193.
- [4] L. Liu, H. Meng, Y. Chai, X. Chen, J. Xu, X. Liu, W. Liu, D.M. Guldi, Y. Zhu, Enhancing built-in electric fields for efficient photocatalytic hydrogen evolution by encapsulating C<sub>60</sub> fullerene into zirconium-based metal–organic frameworks, *Angew. Chem. Int. Ed.* 62 (2023), e202217897.
- [5] C. Zhang, C. Xie, Y. Gao, X. Tao, C. Ding, F. Fan, H.L. Jiang, Charge separation by creating band bending in metal–organic frameworks for improved photocatalytic hydrogen evolution, *Angew. Chem. Int. Ed.* 61 (2022), e202204108.
- [6] X. Li, Q. Zhu, MOF-based materials for photo- and electrocatalytic CO<sub>2</sub> reduction, *EnergyChem* 2 (2020), 100033.
- [7] Q. Wang, D. Astruc, State of the art and prospects in metal–organic framework (MOF)-based and MOF-derived nanocatalysis, *Chem. Rev.* 120 (2020) 1438–1511.
- [8] L. Li, X.S. Wang, T.F. Liu, J. Ye, Titanium-based MOF materials: from crystal engineering to photocatalysis, *Small Methods* 4 (2020) 2000486.
- [9] J. Wang, L. Qiao, H. Nie, H. Huang, Y. Li, S. Yao, M. Liu, Z. Zhang, Z. Kang, T. Lu, Facile electron delivery from graphene template to ultrathin metal–organic layers for boosting CO<sub>2</sub> photoreduction, *Nat. Commun.* 12 (2021) 813.
- [10] L. Sun, M.G. Campbell, M. Dincă, Electrically conductive porous metal–organic frameworks, *Angew. Chem. Int. Ed.* 55 (2016) 3566–3579.
- [11] L. Shi, T. Wang, H. Zhang, K. Chang, X. Meng, H. Liu, J. Ye, An amine-functionalized iron(III) metal–organic framework as efficient visible-light photocatalyst for Cr(vi) reduction, *Adv. Sci.* 2 (2015) 1500006.
- [12] L. Xia, W. Zhou, Y. Xu, Z. Xia, X. Wang, Q. Yang, G. Xie, S. Chen, S. Gao, Ferrocene-boosting Zr-MOFs for efficient photocatalytic CO<sub>2</sub> reduction: A trade-off between enhancing LMCT and frustrating Lewis acid, *Chem. Eng. J.* 451 (2023), 138747.
- [13] X. Wu, L. Gagliardi, D.G. Truhlar, Cerium metal–organic framework for photocatalysis, *J. Am. Chem. Soc.* 140 (2018) 7904–7912.
- [14] W. Li, Y. Wang, J. Chen, N. Hou, Y. Li, X. Liu, R. Ding, G. Zhou, Q. Li, X. Zhou, Y. Mu, Boosting photo-Fenton process enabled by ligand-to-cluster charge transfer excitations in iron-based metal organic framework, *Appl. Catal. B* 302 (2022), 120882.
- [15] J. Nyakuchena, S. Ostresh, D. Streater, B. Pattengale, J. Neu, C. Fiankor, W. Hu, E. D. Kinigstein, J. Zhang, X. Zhang, C.A. Schmuttenmaer, J. Huang, Direct evidence of photoinduced charge transport mechanism in 2D conductive metal organic frameworks, *J. Am. Chem. Soc.* 142 (2020) 21050–21058.
- [16] F. Guo, R.X. Li, S. Yang, X.Y. Zhang, H. Yu, J.J. Urban, W.Y. Sun, Designing heteroatom-codoped iron metal–organic framework for promotional photoreduction of carbon dioxide to ethylene, *Angew. Chem. Int. Ed.* 62 (2023), e202216232.
- [17] L. Sun, C.H. Hendon, M.A. Minier, A. Walsh, M. Dincă, Million-fold electrical conductivity enhancement in Fe<sub>2</sub>(DEBDC) versus Mn<sub>2</sub>(DEBDC) (E = S, O), *J. Am. Chem. Soc.* 137 (2015) 6164–6167.
- [18] Y. Kamakura, P. Chinapang, S. Masaoka, A. Saeki, K. Ogasawara, S.R. Nishitani, H. Yoshikawa, T. Katayama, N. Tamai, K. Sugimoto, D. Tanaka, Semiconductive nature of lead-based metal–organic frameworks with three-dimensionally extended sulfur secondary building units, *J. Am. Chem. Soc.* 142 (2020) 27–32.
- [19] J. Benecke, S. Mangelsen, T.A. Engesser, T. Weyrich, J. Junge, N. Stock, H. Reinsch, A porous and redox active ferrocenedicarboxylic acid based aluminium MOF with a MIL-53 architecture, *Dalton Trans.* 48 (2019) 16737–16743.
- [20] Z. Huang, H. Yu, L. Wang, X. Liu, T. Lin, F. Haq, S.Z. Vatsadze, D.A. Lemenovskiy, Ferrocene-contained metal organic frameworks: From synthesis to applications, *Coordin. Chem. Rev.* 430 (2021), 213737.
- [21] Z. Deng, Y. Guo, Z. Li, X. Wang, X. Peng, Y.J. Zeng, Ferrocenyl metal–organic framework hollow microspheres for in situ loading palladium nanoparticles as a heterogeneous catalyst, *Dalton Trans.* 48 (2019) 8995–9003.
- [22] Z. Deng, H. Yu, L. Wang, J. Liu, K.J. Shea, Ferrocene-based metal–organic framework nanosheets loaded with palladium as a super-high active hydrogenation catalyst, *J. Mater. Chem. A* 7 (2019) 15975–15980.
- [23] R. Rajak, M. Saraf, S.K. Verma, R. Kumar, S.M. Mobin, Dy(III)-based metal–organic framework as a fluorescent probe for highly selective detection of picric acid in aqueous medium, *Inorg. Chem.* 58 (2019) 16065–16074.
- [24] J. Huo, L. Wang, E. Irran, H. Yu, J. Gao, D. Fan, B. Li, J. Wang, W. Ding, A.M. Amin, C. Li, L. Ma, Hollow ferrocenyl coordination polymer microspheres with micropores in shells prepared by ostwald ripening, *Angew. Chem. Int. Ed.* 49 (2010) 9237–9241.
- [25] Z. Fang, Z. Deng, X. Wan, Z. Li, X. Ma, S. Hussain, Z. Ye, X. Peng, Keggin-type polyoxometalates molecularly loaded in Zr-ferrocene metal organic framework nanosheets for solar-driven CO<sub>2</sub> cycloaddition, *Appl. Catal. B* 296 (2021), 120329.
- [26] Z. Deng, C. Fang, X. Ma, X. Li, Y. Zeng, X. Peng, One stone two birds: Zr–Fe metal–organic framework nanosheet for synergistic photothermal and chemodynamic cancer therapy, *ACS Appl. Mater. Inter.* 12 (2020) 20321–20330.
- [27] L. Ai, C. Zhang, L. Li, J. Jiang, Iron terephthalate metal–organic framework: Revealing the effective activation of hydrogen peroxide for the degradation of organic dye under visible light irradiation, *Appl. Catal. B* 148 149 (2014) 191–200.
- [28] L. Shi, T. Wang, H. Zhang, K. Chang, X. Meng, H. Liu, J. Ye, An amine-functionalized iron(III) metal–organic framework as efficient visible-light photocatalyst for Cr(vi) reduction, *Adv. Sci.* 2 (2015) 1500006.
- [29] D. Wang, R. Huang, W. Liu, D. Sun, Z. Li, Fe-Based MOFs for Photocatalytic CO<sub>2</sub> Reduction: Role of Coordination Unsaturated Sites and Dual Excitation Pathways, *ACS Catal.* 4 (2014) 4254–4260.
- [30] Y. An, H. Li, Y. Liu, B. Huang, Q. Sun, Y. Dai, X. Qin, X. Zhang, Photoelectrical, photophysical and photocatalytic properties of Al based MOFs: MIL-53(Al) and MIL-53-NH<sub>2</sub>(Al), *J. Solid Chem.* 233 (2016) 194–198.
- [31] G. Kresse, J. Furthmüller, Efficient iterative schemes for ab initio total-energy calculations using a plane-wave basis set, *Phys. Rev. B* 54 (1996) 11169–11186.
- [32] G. Kresse, J. Furthmüller, Efficiency of ab-initio total energy calculations for metals and semiconductors using a plane-wave basis set, *Comput. Mater. Sci.* 6 (1996) 15–50.
- [33] J.P. Perdew, K. Burke, M. Ernzerhof, Generalized gradient approximation made simple, *Phys. Rev. Lett.* 77 (1996) 3865–3868.
- [34] P. Blöchl, Projector augmented-wave method, *Phys. Rev. B* 50 (1994) 17953–17979.
- [35] G. Kresse, D. Joubert, From ultrasoft pseudopotentials to the projector augmented-wave method, *Phys. Rev. B* 59 (1999) 1758–1775.
- [36] J. Liu, N. Li, J. Sun, J. Liu, L. Dong, S. Yao, L. Zhang, Z. Xin, J. Shi, J. Wang, S. Li, Y. Lan, Ferrocene-Functionalized Polyoxo-Titanium Cluster for CO<sub>2</sub> Photoreduction, *ACS Catal.* 11 (2021) 4510–4519.
- [37] B.A.D. Williamson, J. Buckeridge, J. Brown, S. Ansbro, R.G. Palgrave, D. O. Scanlon, Engineering valence band dispersion for high mobility p-type semiconductors, *Chem. Mater.* 29 (2017) 2402–2413.
- [38] M.Y. Gao, H. Bai, X. Cui, S. Liu, S. Ling, T. Kong, B. Bai, C. Hu, Y. Dai, Y. Zhao, L. Zhang, J. Zhang, Y. Xiong, Precisely tailoring heterometallic polyoxotitanium clusters for the efficient and selective photocatalytic oxidation of hydrocarbons, *Angew. Chem. Int. Ed.* 61 (2022), e2022155.
- [39] H. Feng, X. Liu, Y. Li, X. Ma, Q. Yan, F. Zhao, Novel powder catalysts of ferrocene-based metal–organic framework and their catalytic performance for thermal decomposition of ammonium perchlorate, *Powder Technol.* 397 (2022), 117035.
- [40] H. Zhang, G. Zhai, L. Lei, C. Zhang, Y. Liu, Z. Wang, H. Cheng, Z. Zheng, P. Wang, Y. Dai, B. Huang, Photo-induced photo-thermal synergy effect leading to efficient CO<sub>2</sub> cycloaddition with epoxide over a Fe-based metal organic framework, *J. Colloid Interf. Sci.* 625 (2022) 33–40.
- [41] X. Dao, J. Guo, X. Zhang, S. Wang, X. Cheng, W. Sun, Structure-dependent iron-based metal–organic frameworks for selective CO<sub>2</sub>-to-CH<sub>4</sub> photocatalytic reduction, *J. Mater. Chem. A* 8 (2020) 25850–25856.
- [42] J. Tang, J. Wang, Metal organic framework with coordinatively unsaturated sites as efficient fenton-like catalyst for enhanced degradation of sulfamethazine, *Environ. Sci. Technol.* 52 (2018) 5367–5377.
- [43] Q. Hou, M. Zhen, W. Li, L. Liu, J. Liu, S. Zhang, Y. Nie, C. Bai, X. Bai, M. Ju, Efficient catalytic conversion of glucose into 5-hydroxymethylfurfural by aluminum oxide in ionic liquid, *Appl. Catal. B* 253 (2019) 1–10.
- [44] S. Si, H. Shou, Y. Mao, X. Bao, G. Zhai, K. Song, Z. Wang, P. Wang, Y. Liu, Z. Zheng, Y. Dai, L. Song, B. Huang, H. Cheng, Low-coordination single Au atoms on ultrathin ZnIn<sub>2</sub>S<sub>4</sub> nanosheets for selective photocatalytic CO<sub>2</sub> reduction towards CH<sub>4</sub>, *Angew. Chem. Int. Ed.* 61 (2022), e202209446.
- [45] D. Xiao, X. Bao, M. Zhang, Z. Li, Z. Wang, Y. Gao, Z. Zheng, P. Wang, H. Cheng, Y. Liu, Y. Dai, B. Huang, Stabilizing Cu<sub>2</sub>O for enhancing selectivity of CO<sub>2</sub> electroreduction to C<sub>2</sub>H<sub>4</sub> with the modification of Pd nanoparticles, *Chem. Eng. J.* 452 (2023), 139358.
- [46] Z. Li, B. Sun, D. Xiao, Z. Wang, Y. Liu, Z. Zheng, P. Wang, Y. Dai, H. Cheng, B. Huang, Electron-rich Bi nanosheets promote CO<sub>2</sub><sup>–</sup> formation for high-performance and pH-universal electrocatalytic CO<sub>2</sub> reduction, *Angew. Chem. Int. Ed.* 62 (2023), e202217569.
- [47] Z. Fang, R. Ren, Y. Wang, Y. Hu, M. Dong, Z. Ye, Q. He, X. Peng, Solar-driven all-in-one MOFs-based catalyst for highly efficient CO<sub>2</sub> conversion, *Appl. Catal. B* 318 (2022), 121878.
- [48] J. Xu, H. Xu, A. Dong, H. Zhang, Y. Zhou, H. Dong, B. Tang, Y. Liu, L. Zhang, X. Liu, J. Luo, L. Bie, S. Dai, Y. Wang, X. Sun, Y. Li, Strong electronic metal-support interaction between iridium single atoms and a WO<sub>3</sub> support promotes highly efficient and robust CO<sub>2</sub> cycloaddition, *Adv. Mater.* 34 (2022) 2206991.
- [49] Y. Li, G. Zhai, Y. Liu, Z. Wang, P. Wang, Z. Zheng, H. Cheng, Y. Dai, B. Huang, Synergistic effect between boron containing metal-organic frameworks and light leading to enhanced CO<sub>2</sub> cycloaddition with epoxides, *Chem. Eng. J.* 437 (2022), 135363.
- [50] G. Zhai, Y. Liu, Y. Mao, H. Zhang, L. Lin, Y. Li, Z. Wang, H. Cheng, P. Wang, Z. Zheng, Y. Dai, B. Huang, Improved photocatalytic CO<sub>2</sub> and epoxides cycloaddition via the synergistic effect of Lewis acidity and charge separation over Zn modified UiO-bpydc, *Appl. Catal. B* 301 (2022), 120793.
- [51] Q. Yang, H. Peng, Q. Zhang, X. Qian, X. Chen, X. Tang, S. Dai, J. Zhao, K. Jiang, Q. Yang, J. Sun, L. Zhang, N. Zhang, H. Gao, Z. Lu, L. Chen, Atomically dispersed high-density Al-N<sub>4</sub> sites in porous carbon for efficient photodriven CO<sub>2</sub> cycloaddition, *Adv. Mater.* 33 (2021) 2103186.
- [52] N. Li, X. Zhai, B. Ma, H. Zhang, M. Xiao, Q. Wang, H. Zhang, Highly selective photocatalytic CO<sub>2</sub> reduction via a lead-free perovskite/MOF catalyst, *J. Mater. Chem. A* 11 (2023) 4020–4029.
- [53] W. Liu, L. Li, W. Shao, H. Wang, Y. Dong, M. Zuo, J. Liu, H. Zhang, B. Ye, X. Zhang, Y. Xie, Vacancy-cluster-mediated surface activation for boosting CO<sub>2</sub> chemical fixation, *Chem. Sci.* 14 (2023) 1397–1402.
- [54] Y. Han, Z. Zhou, C. Tian, S. Du, A dual-walled cage MOF as an efficient heterogeneous catalyst for the conversion of CO<sub>2</sub> under mild and co-catalyst free conditions, *Green. Chem.* 18 (2016) 4086–4091.
- [55] L. Gong, J. Sun, Y. Liu, G. Yang, Photoinduced synergistic catalysis on Zn single-atom-loaded hierarchical porous carbon for highly efficient CO<sub>2</sub> cycloaddition conversion, *J. Mater. Chem. A* 9 (2021) 21689–21694.
- [56] Y. Guo, W. Chen, L. Feng, Y. Fan, J. Liang, X. Wang, X. Zhang, Greenery-inspired nanoengineering of bamboo-like hierarchical porous nanotubes with spatially organized bifunctionalities for synergistic photo-thermal catalytic CO<sub>2</sub> fixation, *J. Mater. Chem. A* 10 (2022) 12418–12428.

- [57] C. Duan, Y. Xie, M. Ding, Y. Feng, J. Yao, Design of carbonized melamine sponge@MOFs composites bearing diverse acid-base properties for boosting thermal and solar-driven CO<sub>2</sub> cycloaddition, *J. CO<sub>2</sub> Util.* 64 (2022), 102158.
- [58] Y. Liu, Y. Chen, Y. Liu, Z. Chen, H. Yang, Z. Yue, Q. Fang, Y. Zhi, S. Shan, Zn and N co-doped porous carbon nanosheets for photothermally-driven CO<sub>2</sub> cycloaddition, *J. Catal.* 407 (2022) 65–76.
- [59] Q. Yang, C. Yang, C. Lin, H. Jiang, Metal-organic-framework-derived hollow n-doped porous carbon with ultrahigh concentrations of single Zn atoms for efficient carbon dioxide conversion, *Angew. Chem. Int. Ed.* 58 (2019) 3511–3515.